Catalysis Science & Technology

ROYAL SOCIETY OF CHEMISTRY

PAPER

View Article Online
View Journal | View Issue

Cite this: *Catal. Sci. Technol.*, 2021, 11, 2229

Pyrene-containing conjugated organic microporous polymers for photocatalytic hydrogen evolution from water†

Mohamed Gamal Mohamed, ‡[ab] Mohamed Hammad Elsayed,‡[cd] Ahmed M. Elewa, [c] Ahmed F. M. EL-Mahdy, [a] Cheng-Han Yang,[a] Ahmed A. K. Mohammed,[b] Ho-Hsiu Chou *[c] and Shiao-Wei Kuo *[ae]

Received 30th December 2020,
Accepted 20th January 2021

DOI: 10.1039/d0cy02482a

rsc.li/catalysis

Photoactive conjugated microporous polymers (CMPs) are emerging as porous materials capable of mediating the photocatalytic evolution of H_2 from water. In this study, we synthesized three pyrene-based CMPs (Py–F-CMP, Py–TPA-CMP, Py–TPE-CMP) through Sonogashira–Hagihara cross-couplings of 1,3,6,8-tetraethynylpyrene (Py–T, as a common monomer building block) with 2,7-dibromo-9*H*-fluorene (F–Br_2), tris(4-bromophenyl)amine (TPA–Br_3), and 1,1,2,2-tetrakis(4-bromophenyl)ethene (TPE–Br_4), respectively, in the presence of $Pd(PPh_3)_4$ in DMF/Et_3N. We then characterized the chemical structures, crystallinities, thermal stabilities, surface morphologies, and porosities of these three new CMPs. Brunauer–Emmett–Teller (BET) analyses and tests of photocatalytic H_2 production revealed that Py–TPA-CMP displayed the highest BET surface area (454 $m^2\ g^{-1}$), highest total pore volume (0.28 $cm^3\ g^{-1}$), highest H_2 evolution rate (19 200 μmol $h^{-1}\ g^{-1}$), and highest apparent quantum yield (15.3%) when compared with those of Py–F-CMP, Py–TPE-CMP, and other organic porous materials.

Introduction

Hydrogen (H_2) is perhaps the most environmentally friendly and sustainable energy source for solving our energy crisis and overcoming environmental pollution.[1–6] The production of H_2 can be achieved most simply through photocatalytic water splitting.[4–12] If a polymeric material is to be used as a photocatalyst for water splitting it should possess the following features: (i) corrosion-resistance toward water; (ii) suitable energy levels and structures to facilitate transport of charge carriers in the polymeric framework; (iii) a suitable band gap to enhance the capture of visible photons to produce sufficient carriers to facilitate the reduction of protons; (iv) a suitable absorption band edge position; and (v) an appropriate surface to catalyze chemical reactions.[13–18] Although inorganic semiconductor materials (*e.g.*, oxysulfides, sulfides, metal oxides, nitrides) have been used for photocatalytic H_2 evolution because of their high stability and activity,[17–25] these materials can have their disadvantages, including difficult syntheses, low-availability of their required metal resources, and narrow absorption bands. Fujishima and Honda prepared an operational photo-electrochemical cell featuring a TiO_2 electrode for water spitting.[24] In contrast, Wang and co-workers used g-C_3N_4, a highly thermally and chemically stable metal-free polymer, as a photocatalyst for H_2 production.[25] The search for additional materials that can be used in photocatalytic H_2 production systems has become a hot topic in academia and industry. Organic semiconductor photocatalysts are particularly attractive because of their tunable energy band structures, tunable electronic structures, tunable molecular structures, ease of synthesis, and ease of functional group modification.[26–28] Conjugated microporous polymers (CMPs), linear conjugated polymers, covalent triazine-based frameworks (CTFs), and covalent organic frameworks (COFs) are all organic polymer materials that have been tested widely in photocatalysis, supercapacitors, chemical sensors, CO_2 uptake, optical devices, and photocatalytic H_2 production.[29–48] CMPs are particularly interesting emerging materials for gas storage and conversion, drug delivery, chemical sensing, photocatalysis, photocatalytic CO_2 reduction, optical devices, energy storage, and light-driven H_2 production, due to their tunable permanent nanoporous structures, ease of

[a] *Department of Materials and Optoelectronic Science, Center of Crystal Research, National Sun Yat-Sen University, Kaohsiung 804, Taiwan. E-mail: kuosw@faculty.nsysu.edu.tw*
[b] *Chemistry Department, Faculty of Science, Assiut University, Assiut, 71516, Egypt*
[c] *Department of Chemical Engineering, National Tsing Hua University, Hsinchu 30013, Taiwan. E-mail: hhchou@mx.nthu.edu.tw*
[d] *Department of Chemistry, Faculty of Science, Al-Azhar University, Nasr City 11884, Cairo, Egypt*
[e] *Department of Medicinal and Applied Chemistry, Kaohsiung Medical University, Kaohsiung 807, Taiwan*

† Electronic supplementary information (ESI) available. See DOI: 10.1039/d0cy02482a

‡ These authors contributed equally.

synthesis, low cost, excellent stability and activity, high surface areas and porosities, low densities, diverse material morphologies and compositions, and useful energy level structures, optical band gaps, and photoelectric properties.[49–57] Janiak *et al.* prepared PCTF-8, a CMP that featured a BET surface area (S_{BET}) of 625 m^2 g^{-1}, a total pore volume of 0.32 cm^3 g^{-1}, and a H_2 evolution rate (HER) of 1185 μmol h^{-1} g^{-1} when irradiated with light at wavelengths greater than 420 nm.[58] Cooper *et al.* reported that the CMP S-CMP3 displayed HERs of 3106 and 6076 μmol h^{-1} g^{-1} when irradiated with light at >420 and 251 nm, respectively, with the apparent quantum yield (AQY) reaching 13.2% at 420 nm.[53] Furthermore, Bojdys *et al.* synthesized SNP-2 and found that this CMP material provided a HER of 472 μmol h^{-1} g^{-1} in the presence of Pt and triethanolamine (TEOA) when irradiated with light at 395 nm.[59] Pyrene (Py) moiety possesses extended π-conjugation with planar structure and donor property.[28,60] While triphenylamine (TPA) and its derivatives have central nitrogen atom connected with triphenyl groups, excellent hole transporting and large steric hindrance.[60] The preparation of CMPs based on pyrene, triphenylamine, fluorene (F) and tetraphenylethene (TPE) have been applied as materials in chemical sensing agents, gas adsorbents water treatment, energy storage and optoelectronic devices due to their high specific surface area, easy synthesis, good processability and high thermal stability.[61–66] To the best of our knowledge, the three types of pyrene functionalized CMPs in this study are new and no report until now for using these materials for photocatalytic hydrogen evolution from water. In this study, we prepared the CMPs Py–F-CMP, Py–TPA-CMP and Py–TPE-CMP through Sonogashira–Hagihara cross-couplings of 1,3,6,8-tetraethynylpyrene (as a common monomeric building block) with 2,7-dibromo-9*H*-fluorene (F–Br_2), tris(4-bromophenyl) amine (TPA–Br_3), and 1,1,2,2-tetrakis(4-bromophenyl)ethene (TPE–Br_4), respectively, in the presence of tetrakis(triphenylphosphine) palladium(0) as the catalyst in *N*, *N*-dimethylformamide (DMF)/triethylamine (Et_3N) as the solvent. We then used various techniques to determine the porosities, chemical structures, thermal stabilities, and surface morphologies of these three CMPs. Finally, we measured their abilities to mediate photocatalytic H_2 evolution from water in the presence of ascorbic acid (AA) as a sacrificial electron donor (SED) and Pt as a co-catalyst. These three new CMP materials displayed high H_2 production from water.

Experimental

Materials

Pyrene (98%), triphenylamine (TPA, 98%), (trimethylsilyl) acetylene (98%), copper(I) iodide (CuI, 99%), triphenylphosphine (PPh_3, 99%), *N*-bromosuccinimide (NBS, 99%), benzophenone (99%), bromine (Br_2), zinc (Zn, 98%), titanium tetrachloride ($TiCl_4$, 99.9%), fluorene (98%), potassium carbonate (K_2CO_3, 99.9%), anhydrous ferric chloride ($FeCl_3$, 99.9%), anhydrous Et_3N (99%), anhydrous magnesium sulfate ($MgSO_4$, 99.5%), tetrahydrofuran (THF), acetone, methanol (MeOH), and chloroform ($CHCl_3$) were purchased from Alfa Aesar. $Pd(PPh_3)_4$ was ordered from Sigma-Aldrich.

1,3,6,8-Tetrabromopyrene (Py–Br_4)

A solution of Br_2 (2.3 mL, 44 mmol) was dissolved in nitrobenzene (20 mL) and added to a solution of pyrene (2.00 g, 10 mmol) in nitrobenzene (20 mL). Then the mixture was refluxed at for 4 h at 120 °C until a green powder was appeared. The green solid was washed with EtOH, filtered off, and dried under vacuum at 50 °C under vacuum to Py–Br_4 (4.4 g, 89%). FTIR (KBr, cm^{-1}, Fig. S1†): 3053 (aromatic C–H stretching), 682 (C–Br stretching).

1,3,6,8-Tetrakis(2-(trimethylsilyl)ethynyl)pyrene (Py–TMS)

$Pd(PPh_3)_4$ (220 mg, 0.120 mmol), PPh_3 (244 mg, 0.920 mmol), and CuI (118 mg, 0.620 mmol) were added to a solution of Py–Br_4 (2.00 g, 2.38 mmol) in dry toluene (28 mL) and Et_3N (28 mL) under N_2. After heating to 50 °C, TMSA (2.34 g, 23.8 mmol) was injected dropwise into the flask and then the mixture was heated at for 48 h at 90 °C. The solvent was removed under vacuum to obtain an orange solid. Temperature for onset of decomposition: 350 °C. FTIR (KBr, cm^{-1}, Fig. S2†): 3053 (aromatic C–H stretching), 2908 (aliphatic C–H stretching), 2100 (C≡C stretching), 1618 (C=C stretching). ^{1}H NMR (500 MHz, $CDCl_3$, *δ*, ppm, Fig. S3†): 0.413 (s, 36H, CH_3), 8.3 (s, 2H), 8.57 (s, 4H). ^{13}C NMR (600 MHz, $CDCl_3$, *δ*, ppm, Fig. S4†): 135.70, 132.40, 127.80, 119.20, 103.50, 101.60.

1,3,6,8-Tetraethynylpyrene (Py–T)

A mixture of Py–TMS (2.00 g, 3.41 mmol), K_2CO_3 (5.70 g, 42.0 mmol), and anhydrous MeOH (50 mL) was stirred in a one-neck flask at room temperature for 48 h until an orange powder was formed. The solid was filtered to obtain Py–T (1.88 g, 94.3%; Scheme S1†). Temperature for onset of decomposition: 350 °C. FTIR (KBr, cm^{-1}, Fig. S5†): 3279 (≡C–H), 3065 (aromatic C–H stretching), 2186 (C≡C stretching), 1618 (C=C stretching). ^{1}H NMR (500 MHz, $CDCl_3$, *δ*, ppm, Fig. S6†): 8.68 (s, 4H), 8.38 (s, 2H), 3.67 (s, 4H). ^{13}C NMR (125 MHz, $CDCl_3$, *δ*, ppm, Fig. S7†): 133.80, 130.80, 129.10, 127.80, 84.50, 59.70.

2,7-Dibrmo-9*H*-fluorene (F–Br_2)

$FeCl_3$ (67.0 mg, 1.20 mmol) and fluorene (2.00 g, 12.0 mmol) was dissolved in $CHCl_3$ (25 mL) and then the mixture was cooled in an ice bath at 0 °C. After that, Br_2 solution (1.29 mL, 25.27 mmol) in $CHCl_3$ (15 mL) was injected dropwise to the mixture in the dark. The reaction solution was kept and stirred for at 0 °C for 3 h. Then, saturated aqueous $Na_2S_2O_5$ (40 mL) was added to the reaction mixture. The mixture was extracted with $CHCl_3$ and organic $CHCl_3$ was dried ($MgSO_4$), filtered, and concentrated under vacuum to obtain F–Br_2 as a colorless solid (3.90 g, 89%: Scheme S2†). M.p.: 164–165 °C (DSC, Fig. S8†). FTIR (KBr, cm^{-1}, Fig. S9†): 3051 (aromatic

C–H stretching), 2922 (C–H stretching), 1255 (C–O–C stretching). ^{1}H NMR (500 MHz, $CDCl_3$, δ, ppm, Fig. S10†): 3.04 (s, 2H), 6.94 (d, 2H), 7.06 (d, 2H), 7.57 (d, 2H). ^{13}C NMR (125 MHz, $CDCl_3$, δ, ppm, Fig. S11†): 145.30, 139.80, 131.20, 128.50, 36.50.

Tris(4-bromophenyl)amine (TPA–Br_3)

In a round-bottom flask, NBS (1.00 g, 5.75 mmol) in DMF (10 mL) was mixed with a solution of triphenylamine (TPA) (0.459 g, 1.87 mmol) in DMF (15 mL) and then the mixture was stirred at room temperature for 24 h. After evaporation DMF, CH_2Cl_2 (200 mL) and H_2O (300 mL) were added to the mixture. Then, the organic layer was dried above $MgSO_4$, filtered, and concentrated under vacuum. The residue was washed several times with MeOH to afford TPA–Br_3 as a white solid (0.94 g, 90%: Scheme S3†). M.p.: 140–142 °C (DSC, Fig. S12†). FTIR (KBr, cm^{-1}, Fig. S13†): 3078 (aromatic C–H stretching), 1618 (C═C stretching). ^{1}H NMR (500 MHz, $CDCl_3$, δ, ppm, Fig. S14†): 6.94 (d, 6H), 7.35 (d, 6H). ^{13}C NMR (125 MHz, $CDCl_3$, δ, ppm, Fig. S15†): 146.80, 133.20, 126.20, 116.40.

Tetraphenylethylene (TPE)

Under N_2, benzophenone (3.00 g, 16.4 mmol) and Zn (4.31 g, 65.9 mmol) in THF (80 mL) was stirred in ice/salt-water bath for 10 min. $TiCl_4$ (3.60 mL, 33.0 mmol) was injected over 30 min and then the mixture was kept at 80 °C under reflux. Then, 5% aqueous K_2CO_3 was added to the reaction. After evaporation of the organic solvent, the aqueous phase was extracted three times with EtOAc. After evaporation EtOAc, the residue was washed with EtOH to obtain a white crystalline solid (2.66 g, 97%). M.p.: 228–229 °C (DSC, Fig. S16†). FTIR (KBr, cm^{-1}, Fig. S17†): 3047 (aromatic C–H stretching), 1602 (C═C stretching). ^{1}H NMR (500 MHz, $CDCl_3$, δ, ppm, Fig. S18†): 7.26 (d, 8H), 6.84 (d, 8H). ^{13}C NMR (125 MHz, $CDCl_3$, δ, ppm, Fig. S19†): 140.70, 141.00, 131.30, 127.70, 126.4.

1,1,2,2-Tetrakis(4-bromophenyl)ethene (TPE–Br_4)

A solution of TPE (3.32 g, 10.0 mmol) in glacial acetic acid (10 mL) and CH_2Cl_2 (20 mL) in a round-bottom flask at 0 °C (ice bath). Br_2 (4.00 mL, 80.0 mmol) was added to the mixture and the mixture was kept at room temperature for 48 h. Then, the H_2O (200 mL) was added to the resulting solution and the mixture was extracted with CH_2Cl_2. After evaporation CH_2Cl_2, the residue was washed with MeOH to give a white solid (Scheme S4†), which was recrystallized (CH_2Cl_2/MeOH) to give TPE–Br_4 as a white crystalline solid (6.15 g, 95%). M.p.: 261–262 °C (DSC, Fig. S20†). FTIR (KBr, cm^{-1}, Fig. S21†): 3051 (aromatic C–H stretching), 1572 (C═C stretching). ^{1}H NMR (500 MHz, $CDCl_3$, δ, ppm, Fig. S22†): 7.25 (d, 8H), 6.84 (d, 8H). ^{13}C NMR (125 MHz, $CDCl_3$, δ, ppm, Fig. S23†): 142.30, 139.70, 133.70, 131.90, 121.80.

Py–F-CMP

Py–T (100 mg, 0.340 mmol), F–2Br (174 mg, 0.530 mmol), CuI (6.40 mg, 0.0400 mmol), PPh_3 (14.0 mg, 0.0500 mmol), and $Pd(PPh_3)_4$ (38.0 mg, 0.0330 mmol) in DMF (5 mL) and Et_3N (5 mL) was degassed twice under vacuum and then stirred at 100 °C for 72 h. The insoluble solid was washed several times with THF, DMF, and acetone. The dark red powder was dried at 100 °C (Scheme S5†). FTIR (KBr, cm^{-1}): 3062 (aromatic C–H stretching), 2190 (C≡C stretching), 1603 (C═C stretching).

Py–TPA-CMP

Py–T (100 mg, 0.340 mmol), TPA–Br_3 (216 mg, 0.330 mmol), CuI (6.40 mg, 0.0400 mmol), PPh_3 (14.0 mg, 0.0500 mmol), and $Pd(PPh_3)_4$ (38.0 mg, 0.0330 mmol) in DMF (5 mL) and Et_3N (5 mL) was degassed twice under vacuum and then stirred at 100 °C for 72 h. The insoluble solid was filtered off and washed several times with THF, DMF, and acetone. The dark red powder was dried at 100 °C (Scheme S6†). FTIR (KBr, cm^{-1}): 3058 (aromatic C–H stretching), 2179 (C≡C stretching), 1583 (C═C stretching).

Py–TPE-CMP

Py–T (150 mg, 0.470 mmol), TPE–Br_4 (215 mg, 0.330 mmol), CuI (9.00 mg, 0.0500 mmol), PPh_3 (13.0 mg, 0.0500 mmol), and $Pd(PPh_3)_4$ (57.0 mg, 0.0500 mmol) in DMF (5 mL) and Et_3N (5 mL) was degassed twice under vacuum and then stirred at 100 °C for 72 h. The insoluble solid was filtered off and washed several times with THF, DMF, and acetone. The dark red powder was dried at 100 °C (Scheme S7†). FTIR (KBr, cm^{-1}): 3058 (aromatic C–H stretching), 2179 (C≡C stretching), 1595 (C═C stretching).

Catalyst solution for photocatalytic H_2 evolution

Py–F-CMP, Py–TPA-CMP, or Py–TPE-CMP was dispersed in water/MeOH (2/1, 10 mL) containing H_2PtCl_6 (3%) and 0.1 M AA. The catalyst solution was exposed to light from a 350 W Xe lamp (1000 W m^{-2}; $\lambda > 420$ nm) that had passed through a 420 nm band-pass filter. The production of H_2 was evaluated through gas chromatography (GC7920), operated under the isothermal condition by the semi-capillary column equipped with the thermal conductivity detector. The AQY was calculated using the following equations:

$$\mathrm{AQY} = \frac{\text{number of evolved } H_2 \text{ molecules} \times 2}{\text{number of incident photons}} = \frac{N_e}{N_p} \quad (1)$$

$$= \frac{2M \times N_A}{\frac{E_{total}}{E_{photon}}} = \frac{2M \times N_A}{\frac{S \times P \times t}{h \times \frac{c}{\lambda}}} = \frac{2M \times N_A \times h \times c}{S \times P \times t \times \lambda} \times 100\%$$

where N^A is the Avogadro constant, M is the amount of H_2 produced (mol), c is the speed of light h is the Planck constant, S is the irradiation area (cm^2), t is the photoreaction time (s), P is the intensity of the irradiating light (W cm^{-2}), and λ is the wavelength of the monochromatic light (m).

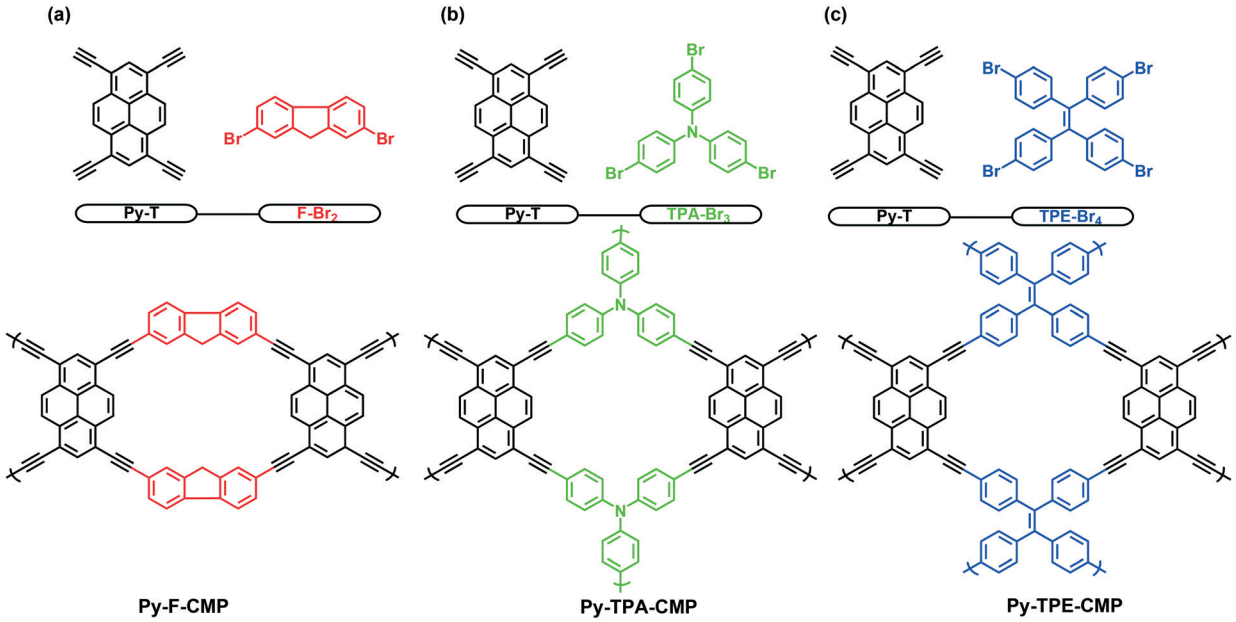

Scheme 1 Synthesis of (a) Py–F-CMP, (b) Py–TPA-CMP, and (c) Py–TPE-CMP through Sonogashira–Hagihara cross-couplings.

Results and discussion

Schemes S1–S4† display the routes followed for the preparation of Py–T, TPE–Br_4, TPA–Br_3, and F–Br_2. The CMPs Py–F-CMP, Py–TPA-CMP, and Py–TPE-CMP were obtained as red solids in high yields through Sonogashira–Hagihara cross-couplings between Py–T (as the common monomer building block) and F–Br_2, TPA–Br_3, and TPE–Br_4, respectively, in the presence of $Pd(PPh_3)_4$ in DMF/Et_3N over 72 h at 100 °C under a N_2 atmosphere (Scheme 1). All the resulting CMP materials are insoluble in DMF, MeOH, EtOH, THF, CH_2Cl_2, DMSO, and acetone. The chemical structures of all the synthesized monomers and of Py–F-CMP, Py–TPA-CMP, and Py–TPE-CMP were confirmed using ^1H and ^{13}C NMR spectroscopy, solid state ^{13}C NMR spectroscopy, and FTIR spectroscopy. The DSC, FTIR and NMR spectra revealed that F–Br_2, TPA–Br_3, TPE and TPE–Br_4 had been obtained with high purity (Fig. S8–S23†). Fig. 1 presents the FTIR spectra of Py–T, Py–F-CMP, Py–TPA-CMP, and Py–TPE-CMP. The FTIR spectrum of Py–T [Fig. 1(a)] features absorption bands at 3279, 3053, 2186, and 1618 cm^{-1}, corresponding to its H–C≡C, C–H aromatic, C≡C, and C=C units, respectively. Fig. 1(b–d) reveals that the signals for the vibrations of the aromatic rings in Py–F-CMP, Py–TPA-CMP, and Py–TPE-CMP appeared clearly in the range 3087–3044 cm^{-1}, while those for the C≡C units appeared in the range 2190–2185 cm^{-1}. Moreover, the large decreases in the intensities of the absorption bands for the terminal alkynyl groups (H–C≡C) near 3279 cm^{-1} in the FTIR spectra of Py–F-CMP, Py–TPA-CMP, and Py–TPE-CMP confirmed that their polymeric condensations had occurred with high degrees of polymerization. Solid state ^{13}C NMR spectroscopy [Fig. 2(a–c)] revealed signals for the carbon nuclei of the aromatic units in the ranges 141.22–120.77 ppm for Py–F-CMP, 146.08–118.53 ppm for Py–TPA-CMP, and 142.19–118.68 ppm for Py–TPE-CMP. In addition, signals of the carbon nuclei of the internal alkynyl bonds of Py–F-CMP, Py–TPA-CMP and Py–TPE-CMP appeared centered at 80.82, 81.95, and 81.39 ppm, respectively. The ^{13}C NMR spectrum of Py–F-CMP [Fig. 2(a)] featured a signal centered at 49.38 ppm for the methylene groups in this framework.

We used thermogravimetric analysis to examine the thermal stabilities of Py–F-CMP, Py–TPA-CMP, and Py–TPE-CMP under a N_2 atmosphere (Fig. 3). The thermal degradation temperatures T_{d5} and T_{d10} of Py–F-CMP were 187 and 321 °C, respectively; for Py–TPA-CMP they were 306 and 382 °C, respectively; and for Py–TPE-CMP they were 295 and 358 °C, respectively. Py–F-CMP, Py–TPA-CMP, and Py–TPE-CMP displayed char yields of 54, 70, and 64%, respectively. The powder X-ray diffraction (PXRD) patterns of these CMPs did not feature any crystalline peaks or long-range order (Fig. S24†), suggesting that each of these materials had amorphous character. We used field-emission scanning electron microscopy (FE-SEM) to examine the surface morphologies of Py–F-CMP, Py–TPA-CMP, and Py–TPE-CMP (Fig. S25†). The surface morphology of Py–F-CMP featured fused rod-like particles, while Py–TPA-CMP and Py–TPE-CMP presented fused irregularly aggregated spherical particles. The BET specific surface areas (S_{BET}), pore diameters, and total pore volumes (V_{total}) of Py–F-CMP, Py–TPA-CMP and Py–TPE-CMP were characterized through N_2 measurements at 77 K (Fig. 4). The BET analyses [Fig. 4(a–c)] revealed type IV curves, suggesting mesoporous structures for these three CMP polymers; furthermore, Fig. 4(b) revealed microporous behavior for Py–TPA-CMP, identified by a sharp rise at relatively low pressure (P/P_0 = 0–0.1). Furthermore, the values of S_{BET} and V_{total} for Py–F-CMP were 191 $m^2\ g^{-1}$ and 0.06 $cm^3\ g^{-1}$, respectively; for Py–TPA-CMP they were 454 $m^2\ g^{-1}$

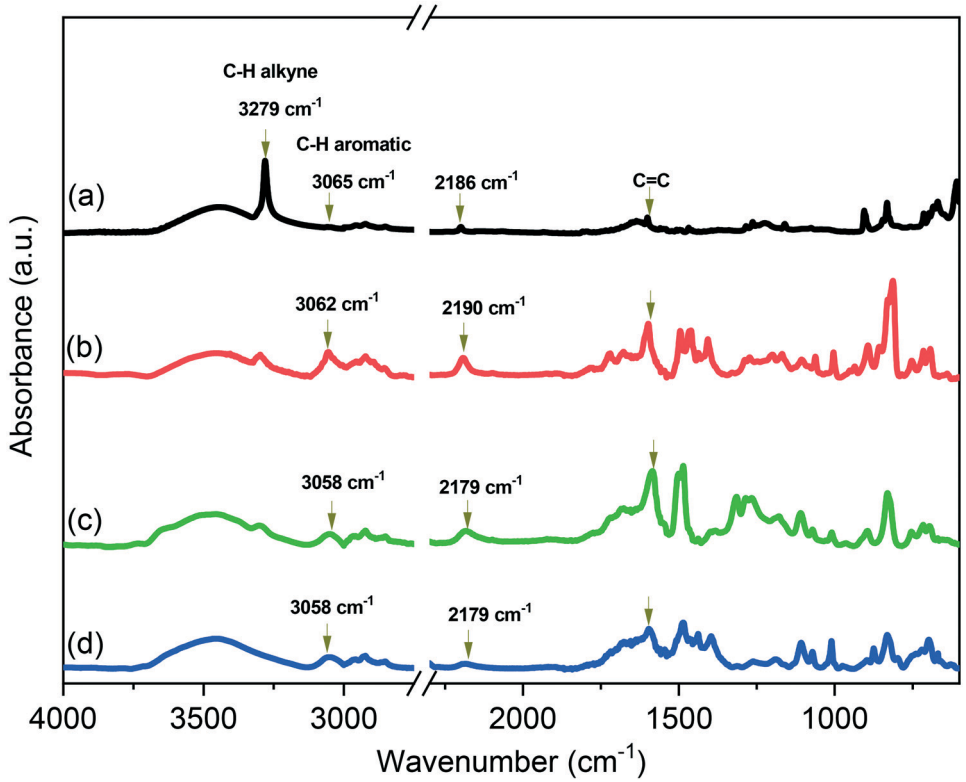

Fig. 1 FTIR spectra of (a) Py–T, (b) Py–F-CMP, (c) Py–TPA-CMP, and (d) Py–TPE-CMP, recorded at 25 °C.

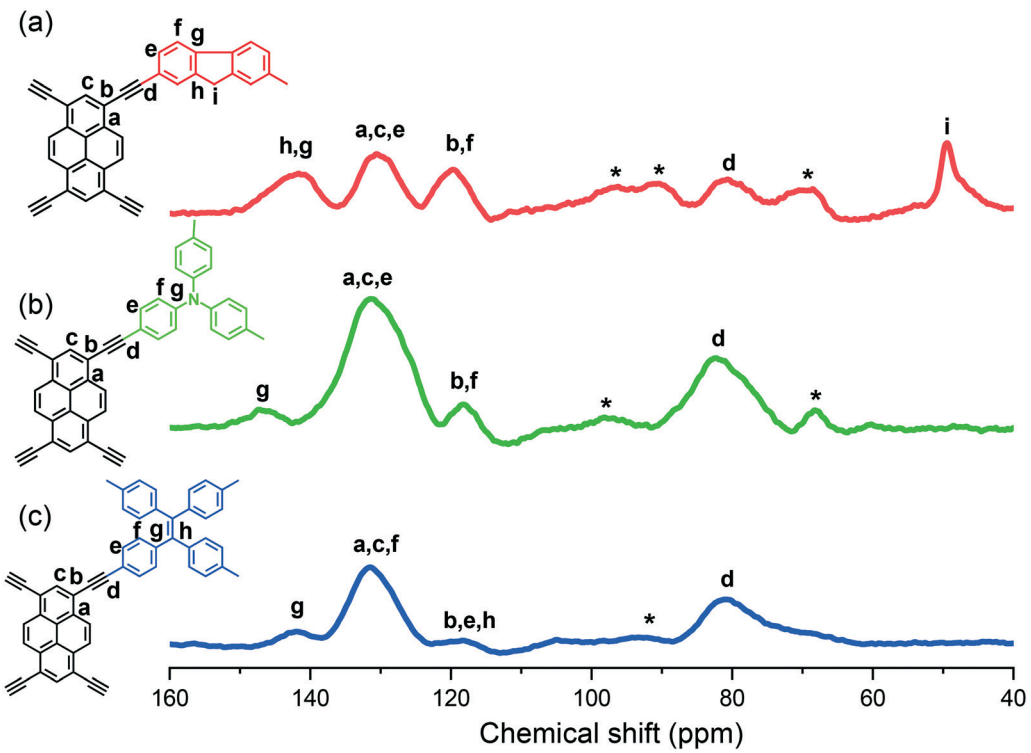

Fig. 2 Solid-state ^{13}C CP/MAS NMR spectra of (a) Py–F-CMP, (b) Py–TPA-CMP, and (c) Py–TPE-CMP, recorded at 25 °C. Asterisks denote spinning sidebands.

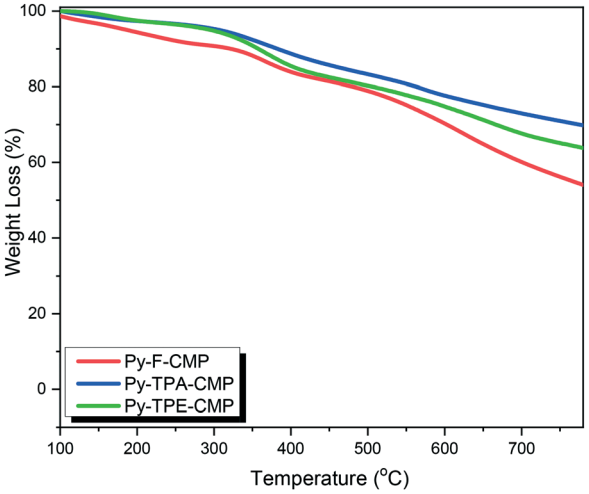

Fig. 3 TGA analyses of Py–F-CMP, Py–TPA-CMP, and Py–TPE-CMP.

and 0.28 $cm^3\ g^{-1}$, respectively; and for Py–TPE-CMP they were 182 $m^2\ g^{-1}$ and 0.13 $cm^3\ g^{-1}$, respectively. We used nonlocal density functional theory (NL-DFT) to evaluate the pore diameters of the CMPs [Fig. 4(d–f)]. Based on their pore size distribution curves, the pore diameters of Py–F-CMP, Py–TPA-CMP, and Py–TPE-CMP were 2.14–2.85, 1.21–2.53, and 2.60 nm, respectively. TEM images [Fig. 4(g–j)] revealed that these three porous polymers possessed micro/mesoporous structures with uniform pore sizes (1.5–2.5 nm). Based on the TGA and BET data, the thermal stability, surface area, and total pore volume of Py–TPA-CMP were all higher than those of Py–F-CMP and Py–TPE-CMP.

We recorded UV-vis diffuse reflectance spectra (DRS) to determine whether the CMPs had optical band gaps suitable for use as photocatalysts; Fig. 5 presents the effective photocatalytic performance of these three polymers. As revealed in Fig. 5(a), all of these polymers absorbed visible light well in the range 350–585 nm. Notably, the signals in

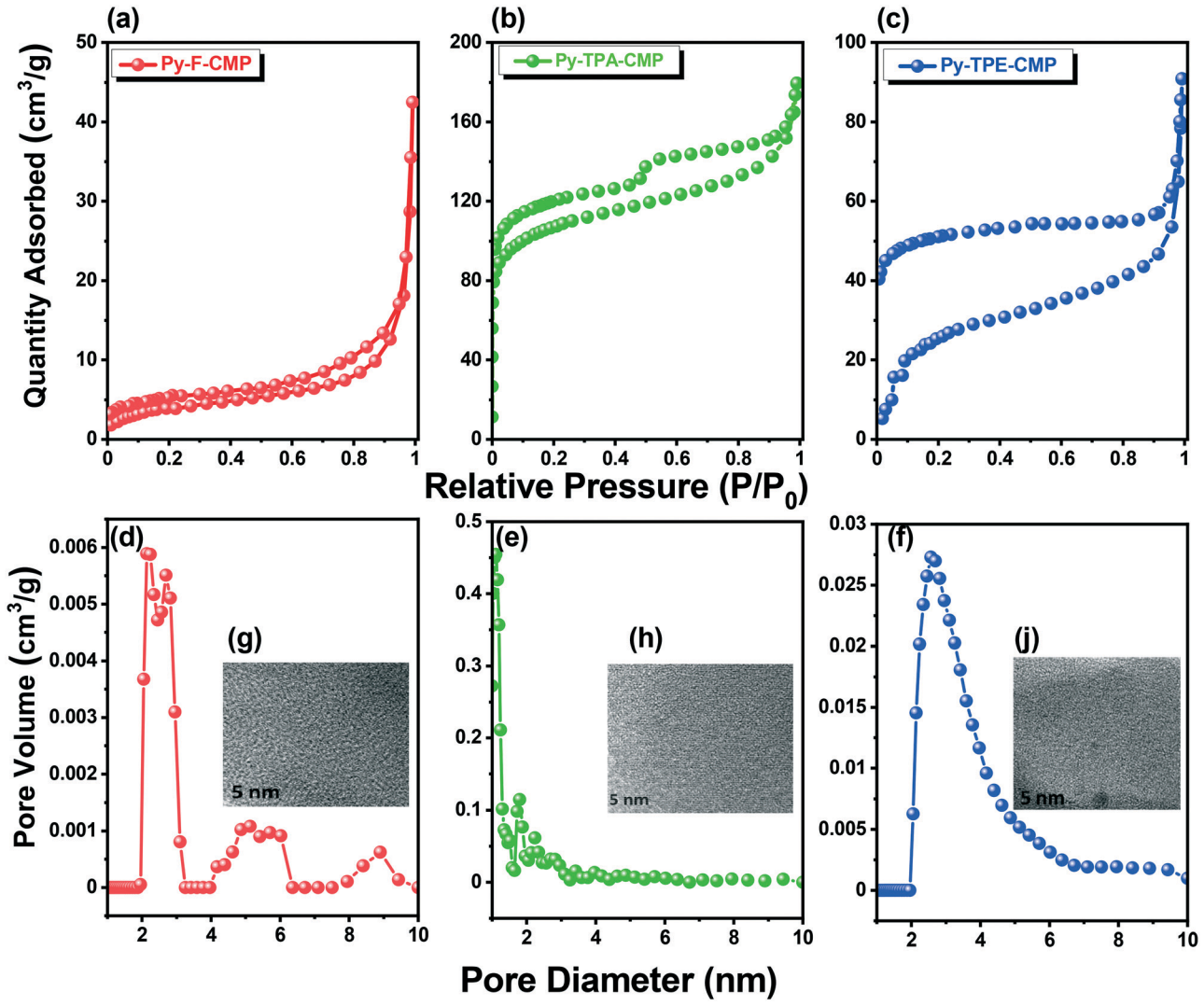

Fig. 4 N_2 adsorption/desorption isotherms of (a) Py–F-CMP, (b) Py–TPA-CMP, and (c) Py–TPE-CMP. Pore size distribution curves of (d) Py–F-CMP, (e) Py–TPA-CMP, and (f) Py–TPE-CMP. TEM images of (g) Py–F-CMP, (h) Py–TPA-CMP, and (j) Py–TPE-CMP.

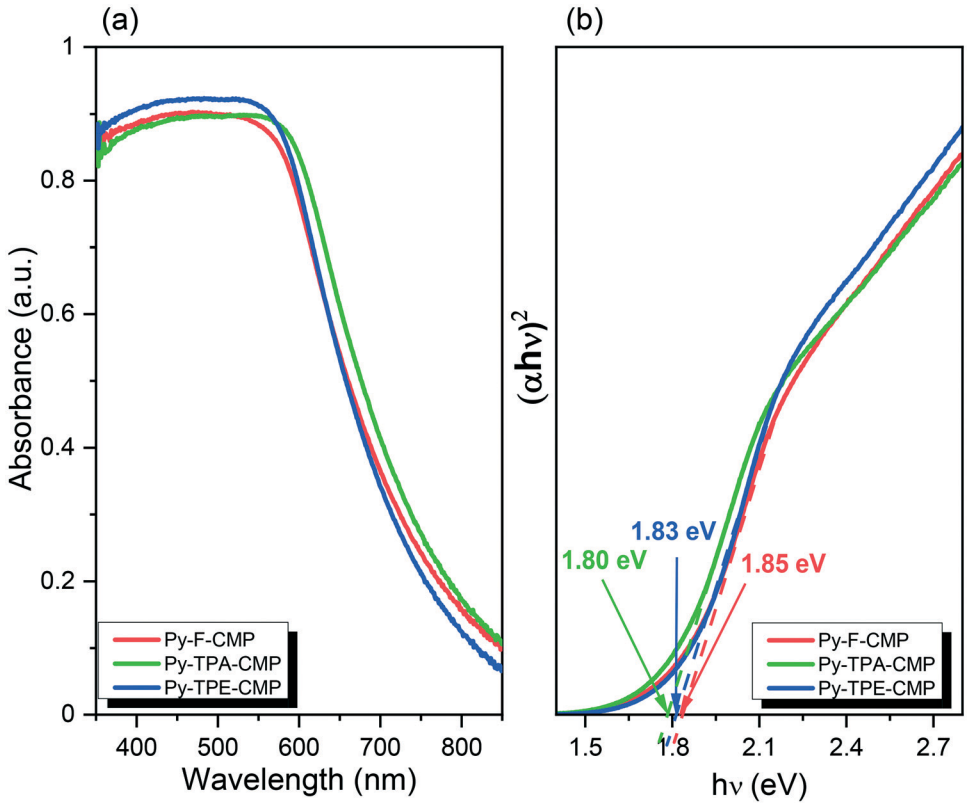

Fig. 5 (a) UV-vis DRS spectra and (b) Tauc plots of $(\alpha h\nu)^2$ *versus* $(h\nu)$, derived from the UV-vis spectral data and by extrapolation from the linear part of the curve to the energy axis based on the equation $\alpha h\nu = A(h\nu - E_g)^{1/2}$, of Py–F-CMP, Py–TPA-CMP, and Py–TPE-CMP.

the spectrum of Py–TPA-CMP were slightly red-shifted when compared with those of Py–F-CMP and Py–TPE-CMP, presumably because of the presence of its TPA units. The optical band gaps of Py–F-CMP, Py–TPA-CMP, and Py–TPE-CMP, calculated from Tauc plots [Fig. 5(b)] were 1.83, 1.80, and 1.85 eV, respectively (Table 1).

Fig. S26† presents the results of photoelectron spectroscopy, revealing that the highest occupied molecular orbitals (HOMOs) of Py–F-CMP, Py–TPA-CMP, and Py–TPE-CMP had energies of 5.65, 5.55, and 5.68 eV, respectively (Table 1); their corresponding lowest unoccupied molecular orbitals (LUMOs) had energies of 3.82, 3.75, and 3.83 eV, respectively (Table 1), calculated from the expression $E_{HOMO} - E_g$ (where E_g was determined using the Tauc plot method).

The UV-vis DRS data suggested that each of these polymers had LUMO energy higher than the potential of water production; therefore, we believed that our three new CMPs would function as photocatalysts for light-driven H_2 evolution. We measured the HER of Py–TPA-CMP in the presence of AA, TEOA, and TEA triethylamine as SEDs, while adding MeOH into the Py–TPA-CMP/H_2O system to enhance the miscibility [Fig. 6(a)]. Py–TPA-CMP displayed good photocatalytic performance in the presence of AA as the SED, with HERs 10-fold and more than 100-fold greater than those obtained using TEOA and TEA, respectively. We optimized various factors to obtain the best conditions for the photocatalytic reaction, including the amount of the photocatalyst, the concentration of Pt co-catalyst, and the concentration of AA as the SED. Fig. 6(b) reveals the effect of the amount of Py–TPA-CMP on the H_2 evolution performance in the presence 0.1 M AA. The HER increased upon increasing the amount of Py–TPA-CMP from 0.5 to 3 mg, but

Table 1 Photophysical properties and H_2 evolution data of the three polymers

Polymer	Absorption [nm]	HOMO/LUMO [eV][a,b]	Band gap [eV][c]	HER [μmol h^{-1}]	HER [μmol h^{-1} g^{-1}]	AQY% at 420 nm (at 460 nm) [%][d,e]
Py–TPA-CMP	360 to 585	−5.55/−3.75	1.80	57.5	19 200	15.3
Py–TPE-CMP	360 to 558	−5.68/−3.83	1.85	39.1	13 033	6.3
Py–F-CMP	360 to 565	−5.65/−3.82	1.83	16.8	5600	2.3

[a] HOMO determined using photoelectron spectroscopy. [b] LUMO derived from the expression $E_{HOMO} - E_g$. [c] Calculated from the Tauc plot of $(\alpha h\nu)^2$ *versus* $(h\nu)$. [d] Conditions: photocatalyst (3 mg), 0.2 M AA, 3% H_2PtCl_6, and 350 W Xe lamp (1000 W m^{-2}; $\lambda > 420$ nm). [e] AQYs measured at 420 and 460 nm.

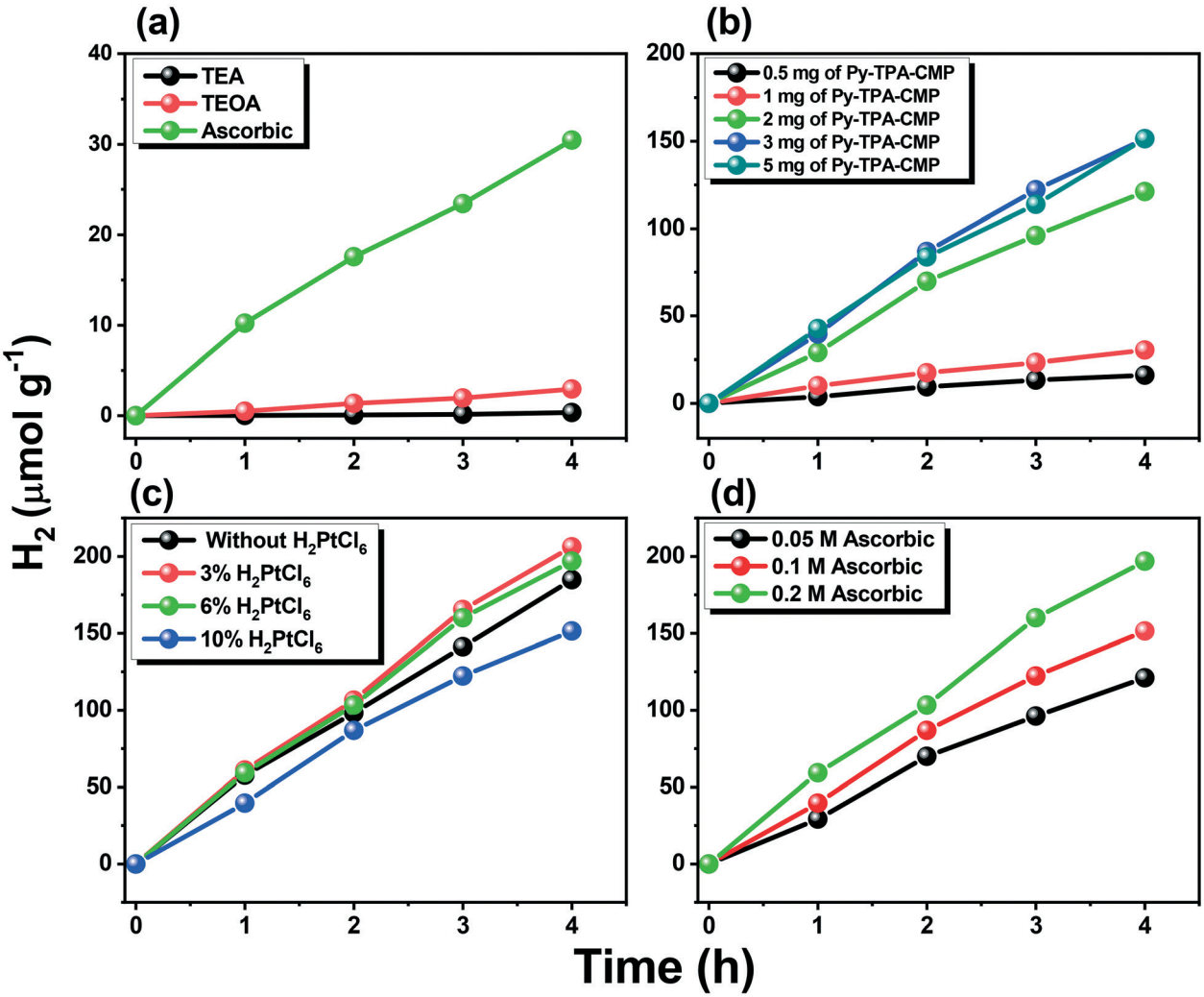

Fig. 6 (a) Effect of SEDs on photocatalytic H_2 production under visible light mediated by Py–TPA-CMP (1 mg); 350 W Xe lamp (1000 W m^{-2}; $\lambda >$ 420 nm). (b) Effect of photocatalyst concentration in the presence of 0.1 M AA; 350 W Xe lamp (1000 W m^{-2}; $\lambda >$ 420 nm). (c) Effect of H_2PtCl_6 as a co-catalyst in the presence of Py–TPA-CMP dose (3 mg) and 0.1 M AA; 350 W Xe lamp (1000 W m^{-2}; $\lambda >$ 420 nm). (d) Effect of AA concentration in the presence of Py–TPA-CMP (3 mg); 350 W Xe lamp (1000 W m^{-2}; $\lambda >$ 420 nm).

it decreased thereafter upon increasing the amount of the CMP to 5 mg, suggesting that the optimum amount of Py–TPA-CMP in this system photocatalytic reaction was 3 mg. Furthermore, the HER of Py–TPA-CMP was enhanced the most in the presence of H_2PtCl_6 when using 3% of this co-catalyst [Fig. 6(c)]. Although Fig. 6(d) reveals that the rate of H_2 production of Py–TPA-CMP also increased upon increasing the AA concentration, we select a concentration of AA of 0.2 M in our subsequent experiments for ready comparison with the results of previous studies. Under the optimal conditions (3 mg of the polymer, 3% Pt, and 0.2 M AA), we compared the performance of the three polymers Py–F-CMP, Py–TPA-CMP, and Py–TPE-CMP as photocatalysts for H_2 evolution under irradiation with visible light ($\lambda >$ 420 nm) at room temperature. As revealed in Fig. 7(a), the amount of generated H_2 reached a maximum value of 231.7 μmol after 6 h when using Py–TPA-CMP as the photocatalyst; this value was higher than those obtained using Py–TPE-CMP (201.9 μmol) and Py–F-CMP (69.1 μmol). Fig. 7(b) and Table 1 display the calculated HERs of our CMPs. The promising HER of Py–TPA-CMP (57.5 μmol h^{-1}) was higher than those of Py–TPE-CMP (39.1 μmol h^{-1}) and Py–F-CMP (16.8 μmol h^{-1}). We attribute the highest HER of Py–TPA-CMP to its high value of S_{BET} (454 m^2 g^{-1}), its high total pore volume (0.28 cm^3 g^{-1}) and its red-shifted UV-vis spectral absorption bands, which enhanced the capture of visible light. In addition, the Py–TPA-CMP contains pyrene as strong electron donating group and TPA as strong electron-accepting unit which can be enhanced the charge separation, and electron transfer ability in the Py–TPA-CMP. Also, the presence of N atom in the TPA units acts as hole traps and provide reactive sites which facilitating hole transfer, charge separation and enhanced H_2 generation from water.[67–69] To evaluate the photocatalytic activity of our photocatalysts for light driven H_2 evolution, we also measured the H_2 evolution from our photocatalytic system in the absence of AA as the SED and also in the absence of the

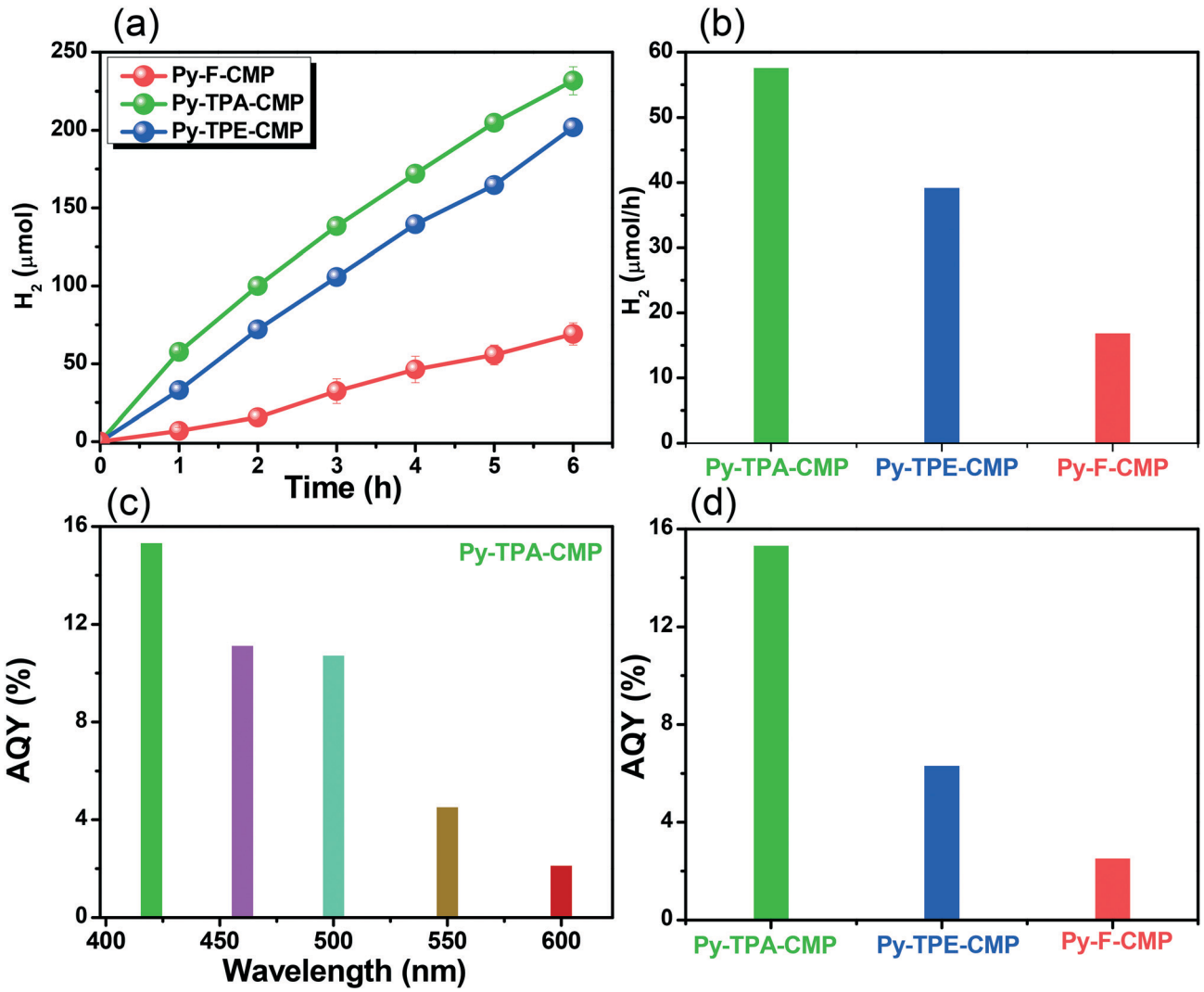

Fig. 7 (a) Time course of the production of H_2 mediated by the three polymers. (b) HERs of the three polymers; conditions: photocatalyst (3 mg), 0.2 M AA, 3% H_2PtCl_6, and 350 W Xe lamp (1000 W m^{-2}; $\lambda > 420$ nm). (c) AQYs of the Py–TPA-CMP at various wavelengths of light. (d) AQYs of the three polymers under light at 420 nm, measured under the optimized conditions at ambient temperature; conditions: photocatalyst (3 mg), 0.2 M AA, 3% H_2PtCl_6, and 350 W Xe lamp (1000 W m^{-2}; $\lambda > 420$ nm).

photocatalyst. As displayed in Fig. S27,† no H_2 production occurred in the absence of AA, light, or polymer under otherwise identical conditions, confirming the necessity of each for a successful photocatalytic process in this system. We also estimated the AQYs of Py–TPA-CMP [Fig. 7(c)] at wavelengths of 420, 460, 500, 550, and 600 nm, obtaining values of 15.3, 11.1, 10.7, 4.5, and 2.1%, respectively. At 420 nm, the AQYs of Py–C-CMP, Py–TPA-CMP, and Py–TPE-CMP were 2.5, 15.3, and 6.3%, respectively [Fig. 7(d)]. Ren *et al.* reported that Ta-CMP-CN, which featured terminal electron withdrawing groups, provided a HER (698 μmol g^{-1} h^{-1}, with an AQY of 0.15%) under visible light that was higher than that of Ta-CMP-N (99 μmol g^{-1} h^{-1}).[70] Wang and co-workers found that the HER of L-PyBT was 87.7 μmol h^{-1}.[71] Table S1† summarizes the HER performances and AQYs of our CMPs and those of the previously reported microporous polymer photocatalysts; among them, our polymers achieved the highest photocatalytic efficiencies and displayed promising AQYs. We employed density functional theory (DFT) to examine the electronic states of our three new polymers. The ground state geometries of the three monomers were optimized using the B3LYP functional with the D3BJ correction and the basis set 6-31G(d). This dispersion correction is necessary to account for long-range and noncovalent interactions.[72,73] Fig. 8 reveals that, for each of the three polymers, both HOMO and LUMO are extended all over the conjugated system. Fig. S28–S30† presented the excited states of the Py–F-CMP, Py–TPA-CMP and Py–TPE-CMP, and their contribution of the transition between orbitals. In addition, Fig. 8 reveals that, for Py–F-CMP and Py–TPE-CMP, the HOMO and LUMO are extended all over the conjugated system. This indicates the complete overlapping for HOMO and LUMO, leads to increasing the recombination of excited electrons. In contrast in the case of Py–TPA-CMP,

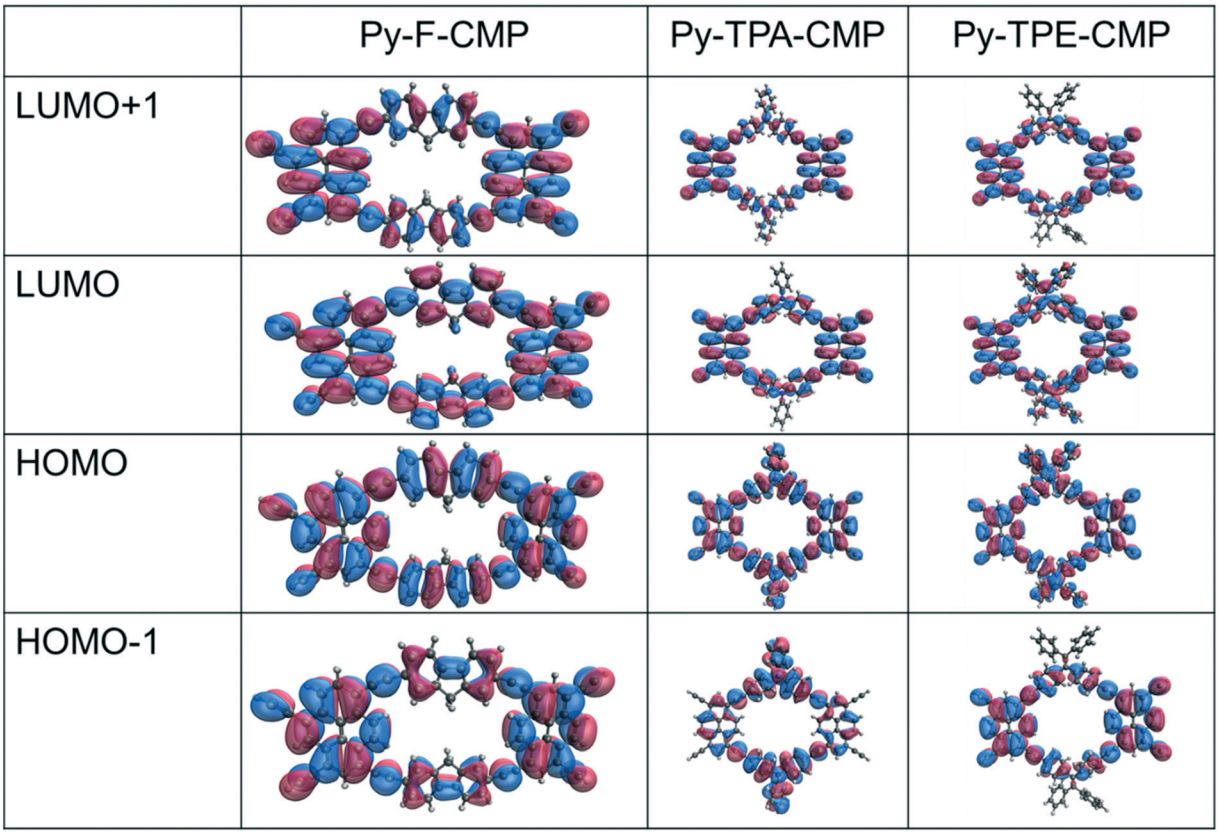

Fig. 8 Main transitions between orbitals that compose the predominant exited state of Py–F-CMP, Py–TPA-CMP and Py–TPE-CMP along with the percentage contribution of each transition.

the LUMO is distributed mostly over the pyrene units, and a lesser extent to TPA unit. Thus, the HOMO and LUMO are partially separated leading to decreasing the recombination of excited electrons and enhancing the photocatalytic efficiency. We tested the stability and recycling of Py–TPA-CMP and Py–TPE-CMP as photocatalysts under irradiation with visible light ($\lambda > 420$ nm) (Fig. S31†). These materials maintained approximately the same performance, in terms of H_2 production rate, over three cycles (18 h) without decreasing the photocatalytic efficiency. Finally, we have performed FTIR and UV-vis measurements, and field-emission scanning electron microscopy (FE-SEM) to check the stability of the chemical structure and surface morphology of Py–F-CMP, Py–TPA-CMP and Py–TPE-CMP after photocatalysts measurements. As shown in FTIR spectra (Fig. S32†), the three new polymers showed absorption bands in the range 3051–3065 cm^{-1}, 2200–2191 cm^{-1}, and 1603–1585 cm^{-1}, corresponding to their C–H aromatic, C≡C, and C=C, respectively. In addition, the absorption bands of Py–F-CMP, Py–TPA-CMP and Py–TPE-CMP were slightly blue-shifted after photocatalysts measurements, as presented in Fig. S33.† Based on SEM images after photocatalysts measurements (Fig. S34†), the surface morphologies of Py–F-CMP, Py–TPA-CMP, and Py–TPE-CMP featured fused rod-like particles. The results above showed that our three polymers could maintain their structure after photocatalytic reaction. Thus, our CMPs function as photocatalysts with promising H_2 production efficiencies and very high stability.

Conclusion

We have synthesized three CMPs—Py–F-CMP, Py–TPA-CMP, and Py–TPE-CMP—based on pyrene moieties through simple and environmentally friendly Sonogashira–Hagihara cross-couplings. FTIR and solid state ^{13}C NMR spectra confirmed their chemical structures. TGA revealed that Py–TPA-CMP had a thermal degradation temperature (358.0 °C) and char yield (70%) higher than those of Py–F-CMP, Py–TPE-CMP, and other porous materials. Furthermore, Py–TPA-CMP provided a HER of 19 200 μmol h^{-1} g^{-1}, with a high AQY of 15.3% that was higher than those of Py–F-CMP and Py–TPE-CMP, presumably because of its high surface area (454 m^2 g^{-1}), high total pore volume (0.28 cm^3 g^{-1}), suitable band gap, and presence of nitrogen heteroatoms.

Conflicts of interest

There are no conflicts to declare.

Acknowledgements

This study was supported financially by the Ministry of Science and Technology, Taiwan, under contracts MOST108-

2638-E-002-003-MY2, 108-2221-E-110-014-MY3 and MOST 109-2636-E-007-021. The authors acknowledge a generous allocation of computer time granted by Compute Canada national HPC platform. The authors thank to the staff at National Sun Yat-sen University for assistance with TEM (ID: EM022600) experiments.

Notes and references

1 L. Hammarström and S. Hammes-Schiffer, Artificial Photosynthesis and Solar Fuels, *Acc. Chem. Res.*, 2009, **42**, 1859–1860.
2 Y. Tachibana and L. Vayssieres, Artificial photosynthesis for solar water-splitting, *Nat. Photonics*, 2012, **6**, 511.
3 J. Zhang, Y. Chen and X. C. Wang, Two-dimensional covalent carbon nitride nanosheets: synthesis, functionalization, and applications, *Energy Environ. Sci.*, 2015, **8**, 3092–3108.
4 Z. A. Lan, W. Ren, X. Chen, Y. F. Zhang and X. C. Wang, Conjugated donor-acceptor polymer photocatalysts with electron-output "tentacles" for efficient hydrogen evolution, *Appl. Catal., A*, 2019, **245**, 596–603.
5 M. Karayilan, W. P. Brezinski, K. E. Clary, D. L. Lichtenberger, R. S. Glass and J. Pyun, Catalytic Metallopolymers from [2Fe-2S] Clusters: Artificial Metalloenzymes for Hydrogen Production, *Angew. Chem.*, 2019, **131**, 7617–7630.
6 K. Mazloomi and C. Gomes, Hydrogen as an energy carrier: Prospects and challenges, *Renewable Sustainable Energy Rev.*, 2012, **16**, 3024–3033.
7 M. H. Elsayed, J. Jayakumar, M. Abdellah, T. H. Mansoure, K. Zheng, A. M. Elewa, C. L. Chang, L. Y. Ting, W. C. Lin, H. H. Yu, W. H. Wang, C. C. Chung and H. H. Chou, Visible-light-driven hydrogen evolution using nitrogen-doped carbon quantum dot-implanted polymer dots as metal-free photocatalysts, *Appl. Catal., B*, 2021, **283**, 119659.
8 M. G. Walter, E. L. Warren, J. R. McKone, S. W. Boettcher, Q. Mi, E. A. Santori and N. S. Lewis, Solar Water Splitting Cells, *Chem. Rev.*, 2010, **110**, 6446–6473.
9 L. Y. Ting, J. Jayakumar, C. L. Chang, W. C. Lin, M. H. Elsayed and H. H. Chou, Effect of controlling the number of fused rings on polymer photocatalysts for visible-light-driven hydrogen evolution, *J. Mater. Chem. A*, 2019, **7**, 22924–22929.
10 P. Kumar, R. Boukherroub and K. Shankar, Sunlight-driven water-splitting using two-dimensional carbon-based semiconductors, *J. Mater. Chem. A*, 2018, **6**, 12876–12931.
11 L. Cheng, Q. Xiang, Y. Liao and H. Zhang, CdS-Based photocatalysts, *Energy Environ. Sci.*, 2018, **11**, 1362–1391.
12 A. F. M. EL-Mahdy, A. M. Elewa, S. W. Huang, H. H. Chou and S. W. Kuo, Dual-Function Fluorescent Covalent Organic Frameworks: HCl Sensing and Photocatalytic H_2 Evolution from Water, *Adv. Opt. Mater.*, 2020, **8**, 2000641.
13 J. Wang, G. Ouyang, Y. Wang, X. Qiao, W. S. Li and H. Li, 1,3,5-Triazine and dibenzo[b,d]thiophene sulfone based conjugated porous polymers for highly efficient photocatalytic hydrogen evolution, *Chem. Commun.*, 2020, **56**, 1601.
14 T. X. Wang, H. P. Liang, D. A. Anito, X. Ding and B. H. Han, Emerging applications of porous organic polymers in visible-light photocatalysis, *J. Mater. Chem. A*, 2020, **8**, 7003–7034.
15 C. L. Chang, W. C. Lin, C. Y. Jia, L. Y. Ting, J. Jayakumar, M. H. Elsayed, Y. Q. Yang, Y. H. Chan, W. S. Wang, C. Y. Lu, P. Y. Chen and H. H. Chou, Low-toxic cycloplatinated polymer dots with rational design of acceptor co-monomers for enhanced photocatalytic efficiency and stability, *Appl. Catal., B*, 2020, **268**, 118436.
16 S. Luo, Z. Zeng, G. Zeng, Z. Liu, R. Xiao, P. Xu, H. Wang, D. Huang, Y. Liu, B. Shao, Q. Liang, D. Wang, Q. He, L. Qin and Y. Fu, Recent advances in conjugated microporous polymers for photocatalysis: designs, applications, and prospects, *J. Mater. Chem. A*, 2020, **8**, 6434.
17 W. H. Wang, L. Y. Ting, J. Jayakumar, C. L. Chang, W. C. Lin, C. C. Chung, M. H. Elsayed, C. Y. Lu, A. M. Elewa and H. H. Chou, Design and synthesis of phenylphosphine oxide-based polymer photocatalysts for highly efficient visible-light-driven hydrogen evolution, Sustain, *Energy Fuels*, 2020, **4**, 5264–5270.
18 W. C. Lin, M. H. Elsayed, J. Jayakumar, L. Y. Ting, C. L. Chang, A. M. Elewa, W. S. Wang, C. C. Chung, C. Y. Lu and H. H. Chou, Design and synthesis of cyclometalated iridium-based polymer dots as photocatalysts for visible light-driven hydrogen evolution, *Int. J. Hydrogen Energy*, 2020, **45**, 32072–32081.
19 R. Asahi, T. Morikawa, H. Irie and T. Ohwaki, Nitrogen-Doped Titanium Dioxide as Visible-Light-Sensitive Photocatalyst: Designs, Developments, and Prospects, *Chem. Rev.*, 2014, **114**, 9824–9852.
20 L. Liu, Z. Ji, W. Zou, X. Gu, Y. Deng, F. Gao, C. Tang and L. Dong, *In Situ* Loading Transition Metal Oxide Clusters on TiO_2 Nanosheets As Co-catalysts for Exceptional High Photoactivity, *ACS Catal.*, 2013, **3**, 2052–2061.
21 X. Chen, S. Shen, L. Guo and S. S. Mao, Semiconductor-based Photocatalytic Hydrogen Generation, *Chem. Rev.*, 2010, **110**, 6503–6570.
22 A. Kudo and Y. Miseki, Heterogeneous photocatalyst materials for water splitting, *Chem. Soc. Rev.*, 2009, **38**, 253–278.
23 L. Liu, X. Gu, Z. Ji, W. Zou, C. Tang, F. Gao and L. Dong, Anion-Assisted Synthesis of TiO_2 Nanocrystals with Tunable Crystal Forms and Crystal Facets and Their Photocatalytic Redox Activities in Organic Reactions, *J. Phys. Chem. C*, 2013, **117**, 18578–18587.
24 A. Fujishima and K. Honda, Electrochemical Photolysis of Water at a Semiconductor Electrode, *Nature*, 1972, **238**, 37–38.
25 X. Wang, K. Maeda, A. Thomas, K. Takanabe, G. Xin, J. M. Carlsson, K. Domen and M. Antonietti, A metal-free polymeric photocatalyst for hydrogen production from water under visible light, *Nat. Mater.*, 2009, **8**, 76.
26 R. S. Sprick, J. X. Jiang, B. Bonillo, S. Ren, T. Ratvijitvech, P. Guiglion, M. A. Zwijnenburg, D. J. Adams and A. I. Cooper, Tunable Organic Photocatalysts for Visible-Light-Driven Hydrogen Evolution, *J. Am. Chem. Soc.*, 2015, **137**, 3265–3270.

27 M. G. Mohamed, C. C. Lee, A. F. M. EL-Mahdy, J. Luder, M. H. Yu, Z. Li, Z. Zhu, C. C. Chueh and S. W. Kuo, Exploitation of Two-Dimensional Conjugated Covalent Organic Frameworks Based on Tetraphenylethylene with Bicarbazole and Pyrene Units and Applications in Perovskite Solar Cells, *J. Mater. Chem. A*, 2020, **8**, 11448–11459.

28 M. G. Mohamed, A. F. M. EL-Mahdy, Y. Takashi and S. W. Kuo, Ultrastable conductive microporous covalent triazine frameworks based on pyrene moieties provide high-performance CO_2 uptake and supercapacitance, *New J. Chem.*, 2020, **44**, 8241–8253.

29 M. G. Mohamed, E. C. A. Jr, B. M. Matsagar, J. Na, Y. Yamauchi, K. C. W. Wu and S. W. Kuo, Construction Hierarchically Mesoporous/Microporous Materials Based on Block Copolymer and Covalent Organic Framework, *J. Taiwan Inst. Chem. Eng.*, 2020, **112**, 180–192.

30 V. S. Vyas, F. Haase, L. Stegbauer, G. Savasci, F. Podjaski, C. Ochsenfeld and B. V. Lotsch, A tunable azine covalent organic framework platform for visible light-induced hydrogen generation, *Nat. Commun.*, 2015, **6**, 8508–8516.

31 A. F. M. EL-Mahdy, M. Y. Lai and S. W. Kuo, Highly fluorescent covalent organic framework as hydrogen chloride sensor: Roles of Schiff base bonding and π-stacking, *J. Mater. Chem. C*, 2020, **8**, 9520–9528.

32 A. F. M. EL-Mahdy, C. H. Kuo, A. Alshehri, C. Young, Y. Yamauchi, J. Kim and S. W. Kuo, Strategic design of triphenylamine- and triphenyltriazine-based two-dimensional covalent organic frameworks for CO_2 uptake and energy storage, *J. Mater. Chem. A*, 2018, **6**, 19532–19541.

33 Y. Yu, N. Mao, S. Feng, C. Zhang, F. Wang, Y. Chen, J. Zeng and J. X. Jiang, Perylene-Containing Conjugated Microporous Polymers for Photocatalytic Hydrogen Evolution, *Macromol. Chem. Phys.*, 2017, **218**, 1700049.

34 C. Krishnaraj, H. S. Jena, K. Leus and P. V. D. Voort, Covalent triazine frameworks a sustainable perspective, *Green Chem.*, 2020, **22**, 1038–1071.

35 X. Wang, K. Maeda, A. Thomas, K. Takanabe, G. Xin, J. M. Carlsson, K. Domen and M. Antonietti, A metal-free polymeric photocatalyst for hydrogen production from water under visible light, *Nat. Mater.*, 2009, **8**, 76–80.

36 A. F. M. El-Mahdy, C. Young, J. Kim, J. You, Y. Yamauchi and S. W. Kuo, Hollow microspherical and microtubular [3+3] carbazole-based covalent organic frameworks and their gas and energy storage applications, *ACS Appl. Mater. Interfaces*, 2019, **11**(9), 9343–9354.

37 B. P. Biswal, H. A. Vignolo-González, T. Banerjee, L. Grunenberg, G. Savasci, K. Gottschling and B. V. Lotsch, Sustained Solar H_2 Evolution from a Thiazolo[5,4-d] thiazole-Bridged Covalent Organic Framework and Nickel-Thiolate Cluster in Water, *J. Am. Chem. Soc.*, 2019, **141**, 11082–11092.

38 A. F. M. EL-Mahdy, Y. H. Hung, T. H. Mansoure, H. H. Yu, Y. S. Hsu, K. C. W. Wu and S. W. Kuo, Synthesis of [3+3] β-ketoenamine-tethered covalent organic frameworks (COFs) for high-performance supercapacitance and CO_2 storage, *J. Taiwan Inst. Chem. Eng.*, 2019, **103**, 199–208.

39 M. M. Samy, M. G. Mohamed and S. W. Kuo, Directly synthesized nitrogen-and-oxygen–doped microporous carbons derived from a bio-derived polybenzoxazine exhibiting high-performance supercapacitance and CO_2 uptake, *Eur. Polym. J.*, 2020, **138**, 109954.

40 L. Li, Z. Cai, Q. Wu, W. Y. Lo, N. Zhang, L. X. Chen and L. Yu, Rational design of porous conjugated polymers and roles of residual palladium for photocatalytic hydrogen production, *J. Am. Chem. Soc.*, 2016, **138**, 7681–7686.

41 M. G. Mohamed, A. F. M. EL-Mahdy, M. M. M. Ahmed and S. W. Kuo, Direct Synthesis of Microporous Bicarbazole-Based Covalent Triazine Frameworks for High-Performance Energy Storage and Carbon Dioxide Uptake, *ChemPlusChem*, 2019, **84**, 1767–1774.

42 D. J. Woods, R. S. Sprick, C. L. Smith, A. J. Cowan and A. I. Cooper, A solution-processable polymer photocatalyst for hydrogen evolution from water, *Adv. Energy Mater.*, 2017, **7**, 1700479.

43 A. F. M. El-Mahdy, M. G. Mohamed, T. H. Mansoure, H. H. Yu, T. Chen and S. W. Kuo, Ultrastable tetraphenyl-p-phenylenediamine-based covalent organic frameworks as platforms for high-performance electrochemical supercapacitors, *Chem. Commun.*, 2019, **55**, 14890–14893.

44 C. B. Meiera, R. S. Sprick, A. Montib, P. Guiglion, J. S. M. Lee, M. A. Zwijnenburg and A. I. Cooper, Structure–property relationships for covalent triazine-based frameworks: the effect of spacer length on photocatalytic hydrogen evolution from water, *Polymer*, 2017, **126**, 283–290.

45 L. Wang, Y. Wan, Y. Ding, S. Wu, Y. Zhang, X. Zhang, G. Zhang, Y. Xiong, X. Wu, J. Yang and H. Xu, Conjugated microporous polymer nanosheets for overall water splitting using visible light, *Adv. Mater.*, 2017, **29**, 1702428.

46 V. S. Vyas, F. Haase, L. Stegbauer, G. Savasci, F. Podjaski, C. Ochsenfeld and B. V. Lotsch, A tunable azine covalent organic framework platform for visible light-induced hydrogen generation, *Nat. Commun.*, 2015, **6**, 8508.

47 M. G. Mohamed, N. Y. Liu, A. F. M. EL-Mahdy and S. W. Kuo, Ultrastable luminescent hybrid microporous polymers based on polyhedral oligomeric silsesquioxane for CO_2 uptake and metal ion sensing, *Microporous Mesoporous Mater.*, 2021, **311**, 110695.

48 T. Sick, A. G. Hufnagel, J. Kampmann, I. Kondofersky, M. Calik, J. M. Rotter, A. Evans, M. Döblinger, S. Herbert, K. Peters, D. Böhm, P. Knochel, D. D. Medina, D. F. Rohlfing and T. Bein, Oriented films of conjugated 2D covalent organic frameworks as photocathodes for water splitting, *J. Am. Chem. Soc.*, 2018, **140**, 2085–2092.

49 P. Pachfule, A. Acharjya, J. Roeser, T. Langenhahn, M. Schwarze, R. Schomäcker, A. Thomas and J. Schmidt, Diacetylene functionalized covalent organic framework (COF) for photocatalytic hydrogen generation, *J. Am. Chem. Soc.*, 2018, **140**, 1423–1427.

50 M. Sachs, R. S. Sprick, D. Pearce, S. A. J. Hillman, A. Monti, A. A. Y. Guilbert, N. J. Brownbill, S. Dimitrov, X. Shi, F. Blanc, M. A. Zwijnenburg, J. Nelson, J. R. Durrant and A. I.

Cooper, Understanding structure-activity relationships in linear polymer photocatalysts for hydrogen evolution, *Nat. Commun.*, 2018, **9**, 4968.

51 Y. Xiang, X. Wang, L. Rao, P. Wang, D. Huang, X. Ding, X. Zhang, S. Wang, H. Chen and Y. Zhu, Conjugated Polymers with Sequential Fluorination for Enhanced Photocatalytic H_2 Evolution via Proton-Coupled Electron Transfer, *ACS Energy Lett.*, 2018, **10**, 2544–2549.

52 X. Wang, B. Chen, W. Dong, X. Zhang, Z. Li, Y. Xiang and H. Chen, Hydrophilicity-Controlled Conjugated Microporous Polymers for Enhanced Visible-Light-Driven Photocatalytic H_2 Evolution, *Macromol. Rapid Commun.*, 2019, **40**, 1800494.

53 R. S. Sprick, Y. Bai, A. A. Y. Guilbert, M. Zbiri, C. M. Aitchison, L. Wilbraham, Y. Yan, D. J. Woods, M. A. Zwijnenburg and A. I. Cooper, Photocatalytic Hydrogen Evolution from Water Using Fluorene and Dibenzothiophene Sulfone-Conjugated Microporous and Linear Polymers, *Chem. Mater.*, 2019, **2**, 305–313.

54 G. Zhang, Z. A. Lan and X. Wang, Conjugated Polymers: Catalysts for Photocatalytic Hydrogen Evolution, *Angew. Chem., Int. Ed.*, 2016, **55**, 15712–15727.

55 C. Dai, L. Zhong, X. Gong, L. Zeng, C. Xue, S. Li and B. Liu, Triphenylamine based conjugated microporous polymers for selective photoreduction of CO_2 to CO under visible light, *Green Chem.*, 2019, **21**, 6606–6610.

56 K. I. Aly, M. M. Sayed, M. G. Mohamed, S. W. Kuo and O. Younis, A facile synthetic route and dual function of network luminescent porous polyester and copolyester containing porphyrin moiety for metal ions sensor and dyes adsorption, *Microporous Mesoporous Mater.*, 2020, **298**, 110063.

57 M. G. Mohamed, X. Zhang, T. H. Mansoure, A. F. M. EL-Mahdy, C. F. Huang, M. Danko, Z. Xin and S. W. Kuo, Hypercrosslinked porous organic polymers based on tetraphenylanthraquinone for CO_2 uptake and high-performance supercapacitor, *Polymer*, 2020, **205**, 122857.

58 A. Bhunia, D. Esquivel, S. Dey, R. Fernandez-Teran, Y. Goto, S. Inagaki, P. Van der Voort and C. Janiak, A photoluminescent covalent triazine framework: CO_2 adsorption, light-driven hydrogen evolution and sensing of nitroaromatics, *J. Mater. Chem. A*, 2016, **4**, 13450–13457.

59 D. Schwarz, Y. S. Kochergin, A. Acharjya, A. Ichangi, M. V. Opanasenko, J. Cejka, U. Lappan, P. Arki, J. He, J. Schmidt, P. Nachtigall, A. Thomas, J. Tarabek and M. J. Bojdys, *Chem. – Eur. J.*, 2017, **23**, 13023–13027.

60 Y. Xu, N. Mao, C. Zhang, X. Wang, J. Zeng, Y. Chen, F. Wang and J. X. Jiang, Rational design of donor-π-acceptor conjugated microporous polymers for photocatalytic hydrogen production, *Appl. Catal., B*, 2018, **228**, 1–9.

61 B. C. Wang, H. R. Liao, J. C. Chang, L. Chen and J. T. Yeh, Electronic structure and molecular orbital study of hole-transport material triphenylamine derivatives, *J. Lumin.*, 2017, **124**, 333–342.

62 M. M. Samy, M. G. Mohamed and S. W. Kuo, Pyrene-functionalized tetraphenylethylene polybenzoxazine for dispersing single-walled carbon nanotubes and energy storage, *Compos. Sci. Technol.*, 2020, **199**, 108360.

63 L. Lan, F. Liu, Y. Dan and L. Jiang, Facile fabrication of triphenylamine-based conjugated porous polymers and their application in organic degradation under visible light, *New J. Chem.*, 2020, **44**, 2986–2995.

64 Q. Zhang, S. Yu, Q. Wang, Q. Xiao, Y. Yue and S. Ren, Fluorene-Based Conjugated Microporous Polymers: Preparation and Chemical Sensing Application, *Macromol. Rapid Commun.*, 2017, **38**, 1700445.

65 M. G. Mohamed, A. F. M. EL-Mahdy, T. S. Meng, M. M. Samy and S. W. Kuo, Multifunctional Hypercrosslinked Porous Organic Polymers Based on Tetraphenylethene and Triphenylamine Derivatives for High-Performance Dye Adsorption and Supercapacitor, *Polymers*, 2020, **12**, 2426.

66 M. G. Mohamed, M. Y. Tsai, C. F. Wang, C. F. Huang, M. Danko, L. Dai, T. Chen and S. W. Kuo, Multifunctional Polyhedral Oligomeric Silsesquioxane (POSS) Based Hybrid Porous Materials for CO_2 Uptake and Iodine Adsorption, *Polymers*, 2021, **13**, 221.

67 S. Bhattacharyya, F. Ehrat, P. Urban, R. Teves, R. Wyrwich, M. Döblinger, J. Feldmann, A. S. Urban and J. K. Stolarczyk, Effect of nitrogen atom positioning on the trade-off between emissive and photocatalytic properties of carbon dots, *Nat. Commun.*, 2017, **8**, 1401.

68 C. Dai and B. Liu, Conjugated polymers for visible-light-driven photocatalysis, *Energy Environ. Sci.*, 2020, **13**, 24–52.

69 J. Yu, X. Sun, X. Xu, C. Zhang and X. He, Donor-Acceptor Type Triazine-based Conjugated Porous Polymer for Visible-Light-Driven Photocatalytic Hydrogen Evolution, *Appl. Catal., B*, 2019, **257**, 117935.

70 K. Ding, Q. Zhang, Q. Li and S. Ren, Terminal Group Effect of Conjugated Microporous Polymers for Photocatalytic Water-Splitting Hydrogen Evolution, *Macromol. Chem. Phys.*, 2019, **220**, 1900304.

71 C. Cheng, X. Wang, Y. Lin, L. He, J. X. Jiang, Y. Xu and F. Wang, The effect of molecular structure and fluorination on the properties of pyrene-benzothiadiazole-based conjugated polymers for visible-light-driven, *Polym. Chem.*, 2018, **9**, 4468–4475.

72 S. Grimme, J. Antony, S. Ehrlich and H. Krieg, A consistent and accurate ab initio parametrization of density functional dispersion correction (DFT-D) for the 94 elements H-Pu, *J. Chem. Phys.*, 2010, **132**, 154104.

73 A. D. Becke and E. R. Johnson, Exchange-hole dipole moment and the dispersion interaction revisited, *J. Chem. Phys.*, 2007, **127**, 154108.